JACS
JOURNAL OF THE AMERICAN CHEMICAL SOCIETY

ARTICLE

pubs.acs.org/JACS

# Unraveling the Mechanism of Nanotube Formation by Chiral Self-Assembly of Amphiphiles

Lior Ziserman,[†] Hee-Young Lee,[§] Srinivasa R. Raghavan,[§] Amram Mor,[†] and Dganit Danino*[,†,‡]

[†]Department of Biotechnology and Food Engineering, and [‡]Russell Berrie Nanotechnology Institute, Technion − Israel Institute of Technology Haifa, Israel, 32000

[§]Department of Chemical and Biomolecular Engineering, University of Maryland, College Park, Maryland 20742-2111, United States

Supporting Information

**ABSTRACT:** The self-assembly of nanotubes from chiral amphi philes and peptide mimics is still poorly understood. Here, we present the first complete path to nanotubes by chiral self-assembly studied with $C_{12}$-$\beta_{12}$ (*N*-α-lauryl-lysyl-aminolauryl-lysyl-amide), a molecule designed to have unique hybrid architecture. Using the technique of direct-imaging cryo-transmission electron microscopy (cryo-TEM), we show the time-evolution from micelles of $C_{12}$-$\beta_{12}$ to closed nanotubes, passing through several types of one-dimensional (1-D) intermediates such as elongated fibrils, twisted ribbons, and coiled helical ribbons. Scattering and diffraction techniques confirm that the fundamental unit is a monolayer lamella of $C_{12}$-$\beta_{12}$, with the hydrophobic tails in the gel state and $\beta$-sheet arrangement. The lamellae are held together by a combination of hydrophobic interactions, and two sets of hydrogen-bonding networks, supporting $C_{12}$-$\beta_{12}$ monomers assembly into fibrils and associating fibrils into ribbons. We further show that neither the "growing width" model nor the "closing pitch" model accurately describe the process of nanotube formation, and both ribbon width and pitch grow with maturation. Additionally, our data exclusively indicate that twisted ribbons are the precursors for coiled ribbons, and the latter structures give rise to nanotubes, and we show chirality is a key requirement for nanotube formation.

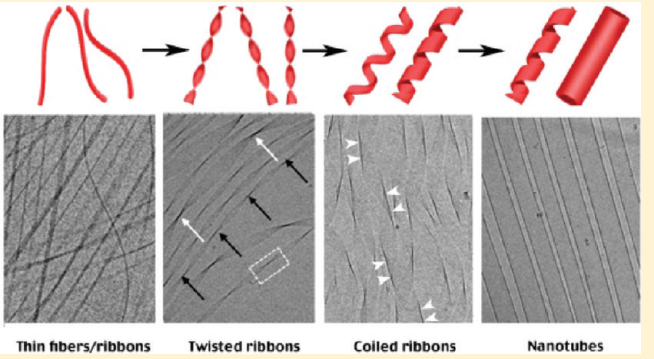


The growing field of nanotechnology has historically emphasized the "bottom-up" approach, in which precursor molecules are able to assemble spontaneously ("self-assemble") into nanostructures of interest when placed in water or other solvents.[1,2] This ability to self-assemble is inherent in biomolecules such as proteins and lipids as well as in synthetic amphiphiles, that is, surfactants and detergents. Although self-assembly has had a long history, there are certain types of self-assembled nanostructures that are much less understood than others. One such class of structures comprises one-dimensional (1-D) typically bilayered aggregates, which encompass fibers, ribbons, and tubes. These structures are formed only by certain chiral amphiphilic molecules and are stable only under a specific set of conditions.

In nature, chiral assembly into supramolecular structures is manifested in many length scales, ranging from 1-D formation of nanotubes by lipids,[3] steroids,[4,5] and their mixtures,[6,7] or collagen self-organization into triple helix fibers,[8] to templating of the chiral property onto the inorganic phase organization at the organism level as in sea shells and insect exoskeletons.[9] Fibrilization is also associated with many human amyloid diseases,[10,11] including Alzheimer, type II diabetes, and multiple sclerosis,[12−15] thus motivating research from various biorelated fields. Apparent advantages of 1-D molecular assemblies, such as structural strength and mechanical rigidity,[16−18] stability, and primarily structural diversity and build-in functionality,[19−26] also foster the application of natural building blocks and their mimics[27] in emerging nanobiotechnology fields. From the pioneering work of Schnur on slow release by lipid nanotubes in the early 1990s,[28] to date, tailor-made lipids, poly peptides, and amphiphilic peptides (AP) were developed as antimicrobial agents,[29] hydrogelators,[18,30,31] and 3-D scaffolds for cell adhesion,[32] molecular recognition, tissue engineering,[33] wound healing,[34] cell−cell communication, and regenerative medicine.[35] In nanotechnology, 1-D assemblies were further used as scaffolds for creating nanowires[36] and nanowires complexes carrying electric signals, for creating layered nanoparticles,[37] as well as for mineralization. Many more applications can be found in recent reviews.[19,20,27,38−40]

1-D tubular assemblies, especially ribbons and nanotubes, are still regarded as exotic structures that fall outside the well-accepted paradigms of the field of self-assembly, as opposed to the self-assembly of amphiphilic molecules into conventional aggregates/phases such as micelles, vesicles, and lyotropic liquid crystals, which is a mature and well-understood subject, discussed at length in textbooks. Indeed, despite extensive experimental and theoretical work, several questions remain to be answered about nanotube formation. In particular, the pathway from conventional aggregates (e.g., micelles or vesicles)

**Received:** August 6, 2010
**Published:** January 18, 2011

**Scheme 1. Molecular Structure of $C_{12}$-$\beta_{12}$ and Its Novel Hybrid Configuration, between Gemini (Two Head−Tail Amphiphiles Linked by a Spacer) and Bolaamphiphile (Two Heads Linked by a Spacer)[a]**

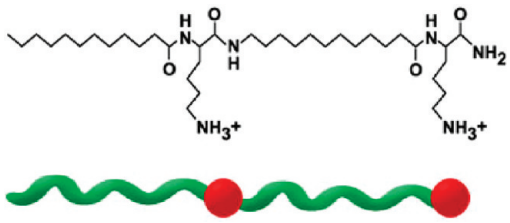

[a] This minimal structure of just two lysine−$C_{12}$ units encodes all prime motifs required for nanotubes formation, chirality, amphiphilicity, and capability of forming hydrogen bonding, as well as hydrophobic chains that, depending on the solution conditions, may behave as amphiphilic tails or as spacers.

into nanotubes has never been elucidated experimentally. To address this, we synthesized a "smart" and simple amino-acid-amphiphile, *N*-α-lauryl-lysyl-aminolauryl-lysyl-amide, referred to as $C_{12}$-$\beta_{12}$ that belongs to a new synthetic library of pseudopeptides termed OAKs[41−43] (for details see Scheme 1), and we investigated the path to nanotubes using cryo-transmission electron microscopy (cryo-TEM). Cryo-TEM has emerged as the premier technique for real-space investigations of self-assembled nanostructures at their native state.[44]

Using time-lapse cryo-TEM, we were able to follow the maturation of structures and resolve the complete self-organization pathway to nanotubes by chiral self-assembly, as depicted in Figure 1. In a fresh $C_{12}$-$\beta_{12}$ solution, within minutes after mixing, numerous fibers and thin ribbons prevail. Image B1 shows they are already many micrometers in length, but <10 nm wide. After a day (image B2), the structures progress into twisted ribbons. Images show the pitch length is relatively uniform along a given ribbon; however, it varies from one ribbon to another (arrowheads). Importantly, we find that twisted ribbons are wider (∼15−25 nm) than the structures in fresh samples, and, furthermore, wider ribbons correlate with longer pitch segments.

After a week, the twisted ribbons had progressed into coiled helical ribbons at various stages of development (image B3). Here, again, it is noted that the helical ribbons are wider than the preceding twisted ribbons. With further incubation, the helical ribbons continue to widen, and, as they do so, the gaps between the coiled pitches began to narrow (image B4).

Complete elimination of these gaps gives rise to nanotubes. Several fully formed nanotubes could be found in 4-week-old samples, but these were still in a minority as compared to the coiled ribbons. It is only in 4-month-old samples that the nanotubes emerge as the dominant structure, as shown in image B5. The nanotubes have a relatively uniform diameter of 70−100 nm, and they show up in the images with clear dark edges, as well as with uniform contrast and no helical markings.

Further insight into the structure of the ribbons shown in Figure 1B2 is provided from an alternate electron microscopy technique, negatively stained TEM (NS-TEM). Low- and high-magnification sections along the ribbon length indicate that the ribbons are a bundle of parallel nanofibers, ∼3−4 nm wide each, as shown in Figure 2A,B.

Having elucidated the pathway to nanotubes using microscopy, we then probed the structure of $C_{12}$-$\beta_{12}$ assemblies at shorter length scales using small-angle neutron scattering (SANS) and wide-angle X-ray diffraction (XRD). Both techniques confirm that the fundamental unit of the fibers, ribbons, and nanotubes is a lamella. As shown in Figure 2C, the plot of SANS intensity $I$ versus wave-vector $q$ at 25 °C shows a slope of −2, which is characteristic of lamellae. Accordingly, a cross-sectional Guinier plot of the same data, that is, a plot of ln $Iq^2$ versus $q^2$ (inset of Figure 2C), falls on a straight line. From the slope of this line, we calculate a lamellar thickness of 2.9 nm, which is comparable with the size of a $C_{12}$-$\beta_{12}$ monolayer, following the fold II arrangement shown in Figure 3A. XRD data obtained on dry powder show a lamellar spacing of reflections in the ratio 1:1/2:1/3:1/4, with the long $d$-spacing being 3.45 nm (Figure 2D). The ratio between reflections is indicative of a lamellar structure. This long $d$-spacing corresponds closely to the total theoretical length of a folded $C_{12}$-$\beta_{12}$ molecule: the sum of contributions from an extended $C_{12}$ chain (1.55 nm), two extended lysines (1.47 nm), and two folded lysines (0.35 nm). The peak at 0.54 nm fits closely the theoretical height of folded $C_{12}$-$\beta_{12}$ that includes one amino-acid amide bond length (0.35 nm) and two C═O bonds (0.124 nm each). The lower value in SANS (as compared to that from powder XRD) may reflect the fact that chiral molecules like $C_{12}$-$\beta_{12}$ do not pack parallel to each other in their lamellae, but rather at a slight tilt with respect to their nearest neighbors.[3,6,45] Regardless, both sets of data support the conclusion that the lamellae are $C_{12}$-$\beta_{12}$ monolayers.

What interactions are responsible for lamella formation? Clearly, hydrophobic interactions are the driving force for the self-organization. To probe additional interactions, we conducted Fourier transform infrared spectroscopy (FTIR) on both aqueous solutions of $C_{12}$-$\beta_{12}$ nanotubes and $C_{12}$-$\beta_{12}$ powder, at 25 °C.[46] The spectra for both samples (Figure 2D) are nearly identical. The relevant peaks include those for amide A at 3293 $cm^{-1}$, amide I at 1676, 1641, and 1623 $cm^{-1}$, and amide II at 1540 $cm^{-1}$, which are indicative of hydrogen bonds. The fact that similar peaks are found in the dry powder as well as in $C_{12}$-$\beta_{12}$ solutions provides evidence for hydrogen bonding (C═O---H−N) between the lysines of adjacent $C_{12}$-$\beta_{12}$ molecules rather than interactions between $C_{12}$-$\beta_{12}$ and water. FTIR also supports the stiff nature of the alkyl chains in $C_{12}$-$\beta_{12}$ nanotubes. That is, the chains are in a stiff all-trans conformation, as indicated by the peaks at 2917 and 2851 $cm^{-1}$, which correspond to $C_{H2}$ antisymmetric and symmetric stretching vibrations, respectively. Analogous peaks are again found in dry $C_{12}$-$\beta_{12}$ as well. Furthermore, amide I band frequencies, known as secondary structure indicators for proteins and peptides, imply $\beta$-sheet ordered supramolecular structure.[23,47−49]

We now address the question of what drives amphiphiles like $C_{12}$-$\beta_{12}$ to assemble into the unusual nanotube architecture rather than spherical vesicles, micelles, and other such common motifs. As shown in Figure 1, $C_{12}$-$\beta_{12}$ forms nanotubes at low temperatures, but not at higher temperatures. A thermogram from DSC shows a single, broad endothermic peak at 30 °C (Figure S1A, Supporting Information), denoted by $T_{g\text{-}l}$, which reflects breaking of the H-bonds and the gel-to-liquid crystalline transition in $C_{12}$-$\beta_{12}$. Above this temperature, the chains are in a fluid, disordered form, whereas below $T_{g\text{-}l}$ the chains are in a frozen or ordered state.[49−51] Based on cryo-TEM analysis, a turbid $C_{12}$-$\beta_{12}$ sample containing nanotubes melts above $T_{g\text{-}l}$ into a transparent solution of spherical micelles, ∼4 nm in diameter (Figure 1C). This transition, we find, is reversible: when the sample is cooled to room temperature, nanotubes form again.

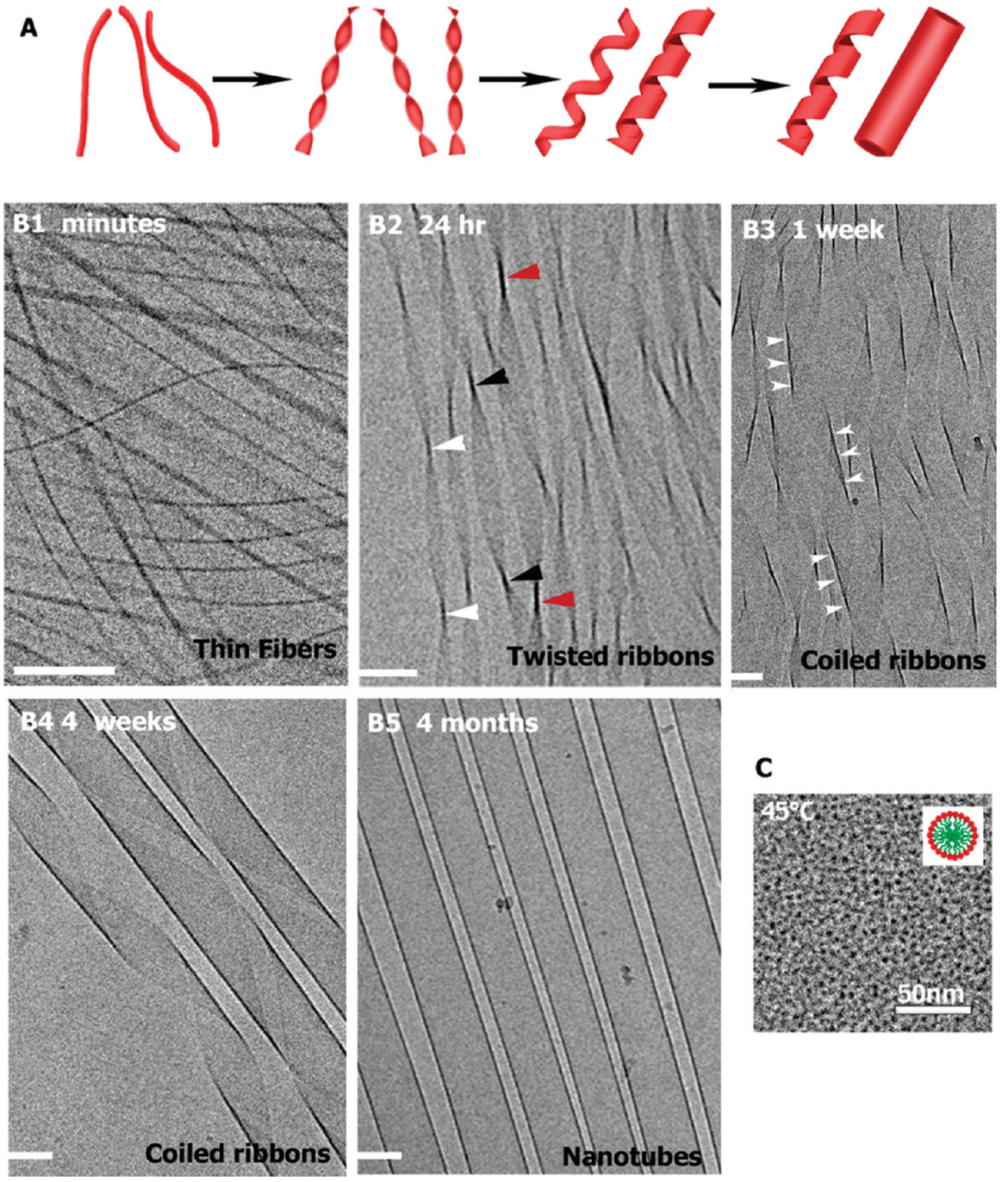


**Figure 1.** Pathway to nanotubes by chiral self-assembly. (A) Schematic illustration of the structures. (B) The pathway as revealed by direct-imaging cryo-TEM. (B1−B5) Time-evolution images of the 1-D supramolecular structures forming at 25 °C. (B1) Thin micrometer-long fibrils in fresh solution. (B2) Twisted ribbons of various widths dominate after overnight incubation. Note the characteristics "bow tie" shape at the twist point. Colored arrowheads that follow the periodicity along the ribbons length show the pitch unit of a single ribbon is fairly uniform, but increases with increase in the ribbon width. (B3) Helically coiled ribbons start to form with aging and comprise the dominant nanostructure between a week (B3) and 4 weeks (B4). Alternating arrowheads follow the helical turn and highlight the cylindrical curvature, as opposed to the Gaussian curvature that characterizes the twisted ribbons shown in B2. The gaps between coils close over time, and after 4 months nanotubes prevail (B5). Bars in B1−B5 = 100 nm. (C) Cryo-TEM image disclosing spherical micelles of ~4 nm at 40 °C, and drawing of the molecular organization within the micelle (inset) showing the micellar hydrophobic core in green and the hydrophilic corona in red.

This reversible transformation and the orientation of $C_{12}$-$\beta_{12}$ molecules within the various structures are explicated in the model presented in Figure 3. In both micelles and lamellae (the basic unit of all tilted structures), the two $C_{12}$ chains are expected to be in close proximity, although with distinct folding due to the hybrid structure of $C_{12}$-$\beta_{12}$. In the fluid phase (above $T_{g\text{-}l}$, where the chains are fluid and H-bonds do not play a role), the two lysine groups are brought closer by folding of the inner acyl chain (spacer) as shown by fold I in Figure 3A. The heads would then get separated from each other, and, in turn, electrostatic


dx.doi.org/10.1021/ja107069f |*J. Am. Chem. Soc.* 2011, 133, 2511–2517

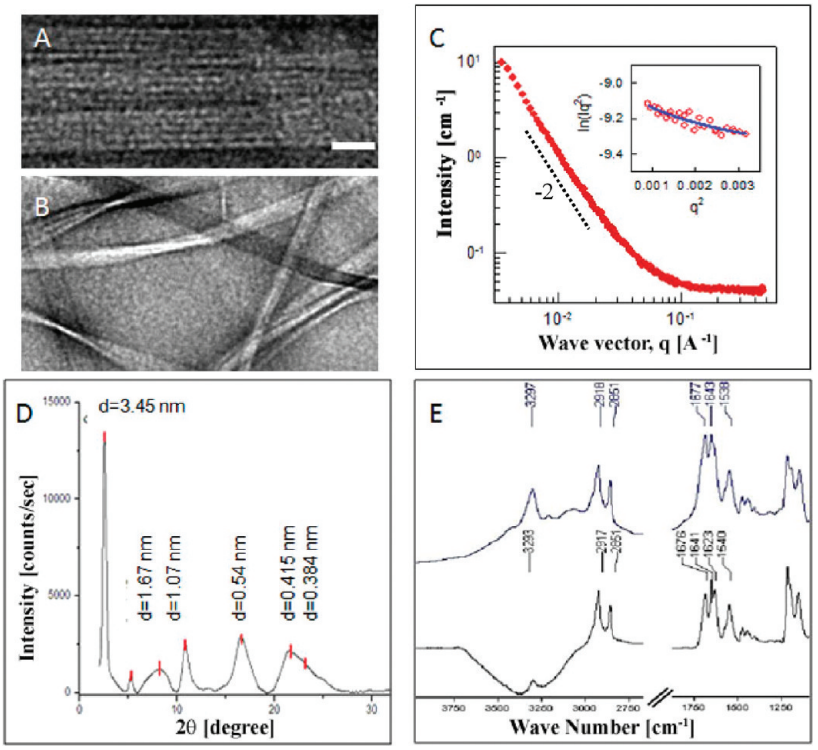


**Figure 2.** Scattering and spectroscopy evidence for molecular monolayer arrangement of $C_{12}$-$\beta_{12}$ at 25 °C and hydrogen bonds. NS-TEM images showing that long fibrilar assemblies held parallel to each other constitute the ribbon elements. Bar equals 25 nm (A) and 50 nm (B). (C) SANS spectra showing the scattered intensity versus wave vector. The $q^{-2}$ decay of the curve is a signature of scattering from a layered structure; Guinier analysis (inset) matches a lamellar thickness of 2.9 nm, in good agreement with the calculated values and the XRD data. (D) Wide-angle XRD measurements of dry $C_{12}$-$\beta_{12}$ powder. Ratio between reflections is consistent with a layered structure. The longest *d* spacing of 3.45 nm correlates with the elements thickness and matches the calculated value from Tanford's equations for fold II shown in Figure 3A. (E) FTIR spectra recorded for both crystalline (dried powder) and aqueous samples (upper and lower plots, respectively) show nearly identical absorption bands, supporting intermolecular hydrogen bonds between lysine groups. FTIR also supports $\beta$-sheet ordered supramolecular structure and stiff (crystalline) all-trans conformation of the chains. Detailed analysis of the peaks is found in the text.

repulsions between the charged lysines become important. Micelle formation in this case, instead of vesicles as with most nanotube-forming amphiphiles, is consistent with the packing parameter concept developed by Israelachvili.[52] The packing parameter links geometrical molecular characteristics with the shape (curvature) of complexes that form by spontaneous self-assembly in solution. It considers hydrophobic interactions, electrostatic forces, and packing constraints and is defined as the ratio of hydrophobic-to-hydrophilic cross-sectional areas, $P = a_{phb}/a_{phl} = v/al$, where $l$ and $v$, the molecule chain length and volume, can be calculated from Tanford's equations. $P$ predicts formation of highly curved spherical micelles like those found in $C_{12}$-$\beta_{12}$ solutions at 40 °C, for $P < 1/3$. In fold I, repulsions effectively enlarge the head area; thus $C_{12}$-$\beta_{12}$ monomer with its bulky head (containing two ion charges) and moderate hydrophobic domain (see Scheme 1 and Figure 3A) will have a small $P$ that will satisfy the creation of small spheres. In these micelles, $C_{12}$-$\beta_{12}$ orients in a way that exposes the two lysine heads (red circles) to water, whereas the two hydrophobic acyls are embedded in the micellar core. Support for fold I is found in our early studies with Gemini amphiphiles,[53] showing that $C_{12}$ linkers are long and flexible enough to fold over and insert into micellar cores. Specifically, the bis(quaternary ammonium bromide) Gemini 12−12−12 (two cation charges like $C_{12}$-$\beta_{12}$ but three $C_{12}$ alkyl chains making it more hydrophobic) organizes into spherical micelles. Moreover, because 12−12−12 is incapable of forming hydrogen bonds, those micelles are stable even at room temperature, and even at concentrations that are more than 100-fold higher.[53] In a hydrophobic Gemini that do form hydrogen bonds, coexistence of spherical micelles and twisted ribbons is reported.[54] Indeed, at short incubation times, spherical micelles are seen in $C_{12}$-$\beta_{12}$ solutions at 25 °C side by side with the fibers and narrow ribbons (Figure 4). This coexistence is also consistent with the broad peak in DSC (Figure S1A, Supporting Information), indicating partial melting of acyl chains and H-bonds already from ∼20 °C.

Such folding of the inner acyl chain is only possible if the hydrocarbon chains are flexible, that is, above $T_{g\text{-}l}$. When $C_{12}$-$\beta_{12}$ micelles are cooled to the gel phase, both hydrocarbon chains stiffen, thus prohibiting such chain folding. Instead, the N-terminal acyl secures maximal hydrophobic contacts by folding back on the second acyl (fold II in Figure 3A), an arrangement naturally leading to a lamella. Note that this is a molecular monolayer because of the specific $C_{12}$-$\beta_{12}$ architecture, and not a bilayer as observed for standard amphiphiles.[50]

## MECHANISM OF CHIRAL SELF-ASSEMBLY INTO NANOTUBES

Hydrophobic interactions are the main driving force for the assembly in the gel phase as well. However, now the molecule assumes a bolaamphiphile configuration. This, together with intermolecular hydrogen bonding between the lysines, act to reduce the effective head area, which further favors the formation of lamellae based on geometric arguments. Thus, driven by hydrophobic interactions and assisted by hydrogen bonds between


dx.doi.org/10.1021/ja107069f |J. Am. Chem. Soc. 2011, 133, 2511–2517

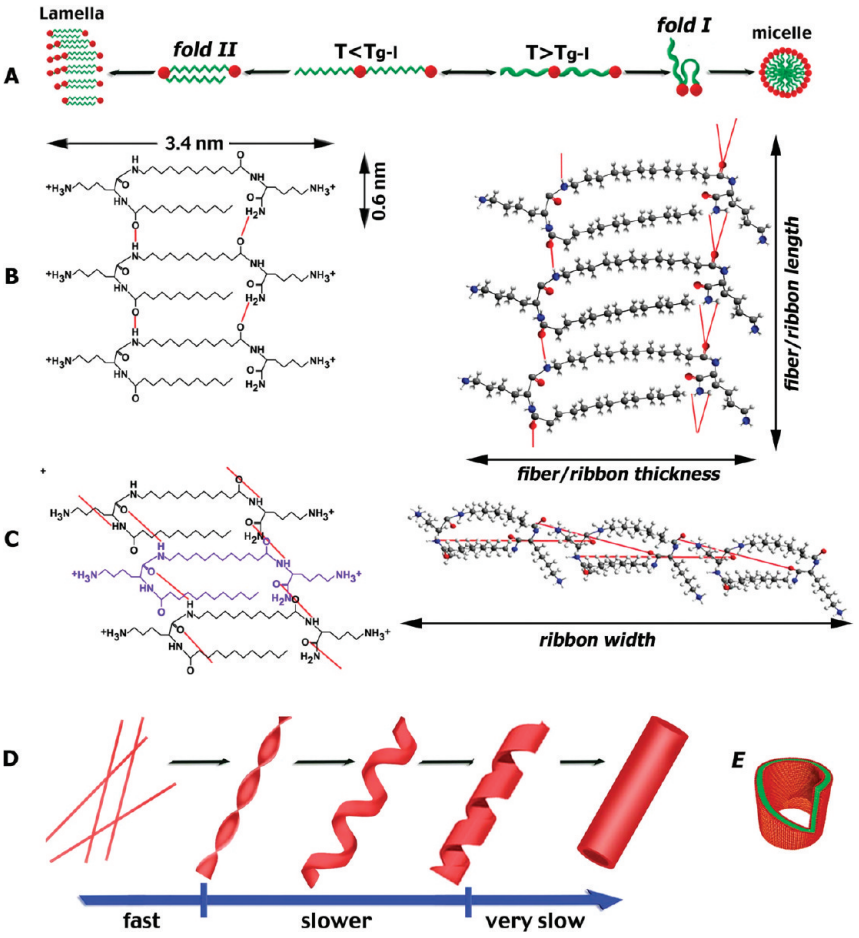


**Figure 3.** Proposed model for the different folding of $C_{12}$-$\beta_{12}$ molecules and inter- and intramolecular H-bondings. (A) In the fluid phase (fold I, 40 °C), the two heads are brought to close proximity by folding of the inner chain. In the gel phase (fold II, 25 °C), the terminal chain folds back to create a bolaamphiphile-like molecule that arranges into a monolayer (fiber) and a lamellar structure (ribbons and nanotubes). (B,C) Models for the organization of molecules into fibers and ribbons; the lattice of fibers follows the ribbons edges. The self-organization into fibers is driven by hydrophobic interactions, and the formed fibers are supported by an intramolecular set of hydrogen bonds along the fibers length (B), and a second, intermolecular set of hydrogen bonds between fibers composing the ribbons and nanotubes (C). (D) Qualitative description of the time-dependent assembly. (E) Section of the nanotube showing the internal hydrophobic domains in (green) and the surface hydrophilic surfaces (in red).

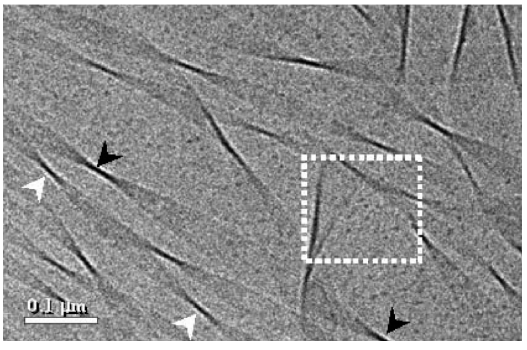


**Figure 4.** Cryo-TEM image of a day-old sample, showing spherical micelles of ~5 nm in diameter (some are enclosed within the white dashed rectangle), coexisting with ribbons. The micelles are a dynamic source of molecules that can advance ribbons widening at the early stages of the assembly. The pair of white arrowheads marks the small pitch of a narrow ribbon, and the pair of black arrowheads marks the large pitch of a wide ribbon.

headgroups of adjacent $C_{12}$-$\beta_{12}$ molecules, the initial aggregation is fast, leading to uniaxial elongation and formation of micrometer-long monolayer fibrils (Figure 1, image B1). Because hydrophobic regions in the monolayer remain exposed to the surrounding solvent, there is also growth along the width direction (Figure 1) that leads to the creation of twisted ribbons, helical ribbons, and finally nanotubes. As the structures widen, the driving force for broadening (e.g., hydrophobic interactions) is decreased, resulting in a slower progression on the way to closed nanotubes (Figure 3D).

Figure 3B and C presents the suggested molecular model for the growth of fibers and their association into ribbons. The lamellae (the basic unit of all tilted structures) are held together by a combination of hydrophobic interactions and intermolecular hydrogen bonding between the lysine heads on adjacent molecules, as evidenced by FTIR. One set of hydrogen bonds, between NH and CO groups that are located relatively far from the lysine residues, supports the length growth (Figure 3B). These groups extend out from the main backbone; thus electrostatic and steric repulsion forces between the lysines of neighboring molecules are small, and H-bonds can easily form and drive instant growth into long fibers, as detected by cryo-TEM. Moreover, the C-terminal $NH_2$ group can potentially form double H-bonds with the carbonyl acceptor, and thus further enhance fast growth along the length.

A second set of hydrogen bonds, between the NH and CO groups that are situated closer to the lysine $C^{\alpha}$, supports the


dx.doi.org/10.1021/ja107069f |J. Am. Chem. Soc. 2011, 133, 2511–2517

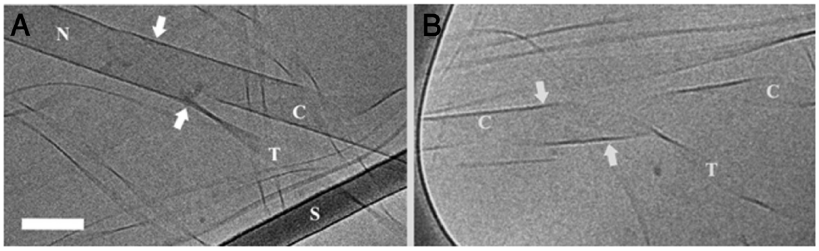


**Figure 5.** Evidence for broadening and maturation of $C_{12}$-$\beta_{12}$ structures through fusion. (A) Twisted ribbon (T) and coiled ribbon (C) fusing into a nanotube (N). (B) Twisted and coiled ribbons fusing to a wider coiled ribbon. Arrows highlight the connections points; the letter "S" marks the carbon support film. Scale bar = 100 nm.

association of fibers into ribbons (Figure 3C). These bonds are less favorable, thus the relatively slow broadening of ribbon with time. The model places the lysine cationic $C^{\varepsilon}$ amine groups on opposite sides of the monolayer to minimize electrostatic repulsions. Finally, we consider further stabilization of the $NH_3$ groups by creation of NH−OH hydrogen bonds with the water, based on FTIR data showing that amide A frequency is lower (indicative of more H-bonds) in solution than in dry powder form.

The overall array of hydrogen bonds is depicted in Figure S1B (Supporting Information). Note that the stiff, regular arrangement of the chains allows the chiral heads to orient in a regular fashion as well, which facilitates the hydrogen bonds between them.

We have found evidence for several mechanisms by which the nanotubes can develop. Cooling to below $T_{g\text{-}l}$ stimulates rapid growth of filaments from spherical micelles, and within minutes they reach micrometers in length (Figure 1B1). Spherical micelles serve also as a dynamic reservoir source for feeding the growth and widening of ribbons at short times. Cryo-TEM images show clearly the presence of many spherical micelles coexisting with filaments and narrow twisted ribbons in fresh samples and after aging overnight (e.g., Figure 4). The micelles' dynamic nature facilitates release of monomers that can readily attach to fibers and ribbons edges. Recent theoretical work shows this widening is coupled with a considerable energy gain.[55] Within a few days, the source of micelles is exhausted as evident from EM, hence ribbon broadening must then continue via a different route. A possible thermodynamically driven mechanism would be Ostwald ripening, which favors the growth of larger elements over the small ones. This may occur via exchange of individual monomers between fibers and ribbons. Alternatively, widening may proceed through the fusion of fibers and ribbons. Figure 5 discloses two examples of connected elements: twisted and helical ribbons connecting into a nanotube (Figure 5A) and twisted and helical ribbons fusing into a wider helical ribbon (Figure 5B). Given that the structures grow over time, we consider these to be fusion events rather than splitting, although the last option cannot be excluded. Importantly, fusion events were seen in both cryo-TEM and negative-stain specimens, ruling out the likelihood that those were introduced during specimen preparation (e.g., during blotting of cryo-TEM samples). Connections of ribbons to the main body of "nanobelts" were recently reported by Stupp,[25] supporting this as a general mechanism.

## TWISTED VERSUS HELICAL RIBBONS

Theories generally distinguish between two types of ribbon morphologies: the twisted ribbon, which has a Gaussian, saddle-like curvature, and the helically coiled ribbon form, which has a cylindrical curvature. Oda and co-workers suggested that a ribbon "must choose" between these two structures.[56] More recent work showed few twisted and helical ribbons in the vicinity of nanotubes.[5,30] In other studies, a transition between the two morphologies could be induced by changing physico-chemical conditions such as temperature or pH, or mixing (multicomponent system).[57] Our detailed investigations show not just the coexistence of twisted ribbons, coiled ribbons, and nanotubes, they exclusively indicate that in this system twisted ribbons are the precursors for coiled ribbons, which subsequently develop into nanotubes. Moreover, we found that this transition in curvature is linked to geometrical parameters of the ribbons, which in our system is a width of ~30 nm. These findings are in agreement with the theoretical study by Buinsma et al.[55] To our knowledge, this is the first experimental clarification of the combined roles played by twisted and coiled ribbons in nanotube formation. Accordingly, in all fusion events seen by us and others,[25] thin ribbons have a Gaussian curvature, while wide ribbons are helical.

## "CLOSING PITCH" AND "GROWING WIDTH" MODELS

Theories on nanotube formation generally assume that helically coiled ribbons may grow into nanotubes by one of two routes.[50] In the "closing pitch model", the ribbon width remains constant, while the pitch of the ribbon gradually shortens until a closed tube is formed. In the second, "growing width model", the helical pitch remains constant, while the ribbons gradually widen until the closed nanotube is formed. In the case of $C_{12}$-$\beta_{12}$, our cryo-TEM results indicate closing of nanotubes when the ribbons widen and eliminate the gaps between their pitches. However, we further found that both the width and the ribbon pitch grow with time (Figure 1, images in B, and Figure 4). Further discussion of this finding is given elsewhere.[58]

## ASSOCIATED CONTENT

**Supporting Information.** Experimental details, DSC data, and the complete molecular-level model for the arrangement of $C_{12}$-$\beta_{12}$. This material is available free of charge via the Internet at http://pubs.acs.org.

## AUTHOR INFORMATION

**Corresponding Author**
dganitd@tx.technion.ac.il

## ACKNOWLEDGMENT

D.D. acknowledges the generous support of RBNI in the study. This research was partly supported by the Israel Science Foundation (grant 283/08 to A.M.).

## REFERENCES


(1) Whitesides, G. M.; Mathias, J. P.; Seto, C. T. *Science* **1991**, *254*, 1312–1319.
(2) Zhang, L. F.; Eisenberg, A. *Polym. Adv. Technol.* **1998**, *9*, 677–699.
(3) Selinger, J. V.; Schnur, J. M. *Phys. Rev. Lett.* **1993**, *71*, 4091–4094.
(4) Terech, P.; de Geyer, A.; Struth, B.; Talmon, Y. *Adv. Mater.* **2002**, *14*, 495–498.
(5) Jean, B.; Oss-Ronen, L.; Terech, P.; Talmon, Y. *Adv. Mater.* **2005**, *17*, 728–731.
(6) Chung, D. S.; Benedek, G. B.; Konikoff, F. M.; Donovan, J. M. *Proc. Natl. Acad. Sci. U.S.A.* **1993**, *90*, 11341–11345.
(7) Konikoff, F. M.; Danino, D.; Weihs, D.; Rubin, M.; Talmon, Y. *Hepatology* **2000**, *31*, 261–268.
(8) Prins, L. J.; Huskens, J.; de Jong, F.; Timmerman, P.; Reinhoudt, D. N. *Nature* **1999**, *398*, 498–502.
(9) Li, C. M.; Kaplan, D. L. *Curr. Opin. Solid State Mater. Sci.* **2003**, *7*, 265–271.
(10) Nelson, R.; Sawaya, M. R.; Balbirnie, M.; Madsen, A. O.; Riekel, C.; Grothe, R.; Eisenberg, D. *Nature* **2005**, *435*, 773–778.
(11) Sawaya, M. R.; Sambashivan, S.; Nelson, R.; Ivanova, M. I.; Sievers, S. A.; Apostol, M. I.; Thompson, M. J.; Balbirnie, M.; Wiltzius, J. J. W.; McFarlane, H. T.; Madsen, A. O.; Riekel, C.; Eisenberg, D. *Nature* **2007**, *447*, 453–457.
(12) Jimenez, J. L.; Nettleton, E. J.; Bouchard, M.; Robinson, C. V.; Dobson, C. M.; Saibil, H. R. *Proc. Natl. Acad. Sci. U.S.A.* **2002**, *99*, 9196–9201.
(13) Soreq, H.; Gazit, E. *Curr. Alzheimer Res.* **2008**, *5*, 232–232.
(14) Selkoe, D. J. *Nature* **1991**, *354*, 432–433.
(15) Selkoe, D. J. *Neuron* **1991**, *6*, 487–498.
(16) Kol, N.; Adler-Abramovich, L.; Barlam, D.; Shneck, R. Z.; Gazit, E.; Rousso, I. *Nano Lett.* **2005**, *5*, 1343–1346.
(17) Smith, J. F.; Knowles, T. P. J.; Dobson, C. M.; MacPhee, C. E.; Welland, M. E. *Proc. Natl. Acad. Sci. U.S.A.* **2006**, *103*, 15806–15811.
(18) Mahler, A.; Reches, M.; Rechter, M.; Cohen, S.; Gazit, E. *Adv. Mater.* **2006**, *18*, 1365–1370.
(19) Zhang, S. G. *Nat. Biotechnol.* **2003**, *21*, 1171–1178.
(20) Gazit, E. *Chem. Soc. Rev.* **2007**, *36*, 1263–1269.
(21) Vos, M. R. J.; Jardl, G. E.; Pallas, A. L.; Breurken, M.; van Asselen, O. L. J.; Bomans, P. H. H.; Leclere, P. E. L. G.; Frederik, P. M.; Nolte, R. J. M.; Sommerdijk, N. A. J. M. *J. Am. Chem. Soc.* **2005**, *127*, 16768–16769.
(22) Bucak, S.; Cenker, C.; Nasir, I.; Olsson, U.; Zackrisson, M. *Langmuir* **2009**, *25*, 4262–4265.
(23) Hamley, I. W.; Castelletto, V.; Moulton, C.; Myatt, D.; Siligardi, G.; Oliveira, C. L. P.; Pedersen, J. S.; Abutbul, I.; Danino, D. *Macromol. Biosci.* **2010**, *10*, 40–48.
(24) Jadhav, S. R.; Vemula, P. K.; Kumar, R.; Raghavan, S. R.; John, G. *Angew. Chem., Int. Ed.*, in press.
(25) Cui, H.; Muraoka, T.; Cheetham, A. G.; Stupp, S. I. *Nano Lett.* **2009**, *9*, 945–951.
(26) Castelletto, V.; Hamley, I. W.; Perez, J.; Abezgauz, L.; Danino, D. *Chem. Commun.* **2010**, *46*, 9185−9187.
(27) Toksoz, S.; Guler, M. O. *Nano Today* **2009**, *4*, 458–469.
(28) Schnur, J. M. *Science* **1993**, *262*, 1669–1676.
(29) Zhou, Y.; Kogiso, M.; Asakawa, M.; Dong, S.; Kiyama, R.; Shimizu, T. *Adv. Mater.* **2009**, *21*, 1742–1745.
(30) Terech, P.; Friol, S.; Sangeetha, N.; Talmon, Y.; Maitra, U. *Rheol. Acta* **2006**, *45*, 435–443.
(31) Rughani, R. V.; Lamm, M. S.; Pochan, D. J.; Schneider, J. P. *Biopolymers* **2007**, *88*, 629–629.
(32) Storrie, H.; Guler, M. O.; Abu-Amara, S. N.; Volberg, T.; Rao, M.; Geiger, B.; Stupp, S. I. *Biomaterials* **2007**, *28*, 4608–4618.
(33) Dinca, V.; Kasotakis, E.; Catherine, J.; Mourka, A.; Ranella, A.; Ovsianikov, A.; Chichkov, B. N.; Farsari, M.; Mitraki, A.; Fotakis, C. *Nano Lett.* **2008**, *8*, 538–543.
(34) Schneider, A.; Garlick, J. A.; Egles, C. *PloS One* **2008**, *3*, e1410.
(35) Holmes, T. C.; de Lacalle, S.; Su, X.; Liu, G. S.; Rich, A.; Zhang, S. G. *Proc. Natl. Acad. Sci. U.S.A.* **2000**, *97*, 6728–6733.
(36) Reches, M.; Gazit, E. *Science* **2003**, *300*, 625–627.
(37) Lamm, M. S.; Sharma, N.; Rajagopal, K.; Beyer, F. L.; Schneider, J. P.; Pochan, D. J. *Adv. Mater.* **2008**, *20*, 447–451.
(38) Frkanec, L.; Zinic, M. *Chem. Commun.* **2010**, *46*, 522–537.
(39) Cao, H. Q.; Liu, T.; Chew, S. Y. *Adv. Drug Delivery Rev.* **2009**, *61*, 1055–1064.
(40) Shimizu, T. *J. Polym. Sci., Part A: Polym. Chem.* **2008**, *46*, 2601–2611.
(41) Radzishevsky, I. S.; Kovachi, T.; Porat, Y.; Ziserman, L.; Zaknoon, F.; Danino, D.; Mor, A. *Chem. Biol.* **2008**, *15*, 354–362.
(42) Rotem, S.; Mor, A. *BBA* **2009**, *1788*, 1582–1592.
(43) Radzishevsky, I. S.; Rotem, S.; Bourdetsky, D.; Navon-Venezia, S.; Carmeli, Y.; Mor, A. *Nat. Biotechnol.* **2007**, *25*, 657–659.
(44) Danino, D.; Bernheim-Groswasser, A.; Talmon, Y. *Colloids Surf., A* **2001**, *183*, 113–122.
(45) Selinger, J. V.; MacKintosh, E. C.; Schnur, J. M. *Phys. Rev. E* **1996**, *53*, 3804–3818.
(46) Krysmann, M. J.; Castelletto, V.; Kelarakis, A.; Hamley, I. W.; Hule, R. A.; Pochan, D. J. *Biochemistry* **2008**, *47*, 4597–4605.
(47) Stuart, B. *Biological Applications of Infrared Spectroscopy*; Wiley: New York, 1997.
(48) Rubin, N.; Perugia, E.; Wolf, S. G.; Klein, E.; Fridkin, M.; Addadi, L. *J. Am. Chem. Soc.* **2010**, *132*, 4242–4248.
(49) Imae, T.; Takahashi, Y.; Muramatsu, H. *J. Am. Chem. Soc.* **1992**, *114*, 3414–3419.
(50) Shimizu, T.; Masuda, M.; Minamikawa, H. *Chem. Rev.* **2005**, *105*, 1401–1443.
(51) Vos, M. R. J.; Leclere, P. E. L. G.; Meekes, H.; Vlieg, E.; Nolte, R. J. M.; Sommerdijk, N. A. J. M. *Chem. Commun.* **2010**, *46*, 6063–6065.
(52) Israelachvili, J. N.; Mitchell, D. J.; Ninham, B. W. *J. Chem. Soc., Faraday Trans. 2* **1976**, *72*, 1525–1568.
(53) Danino, D.; Talmon, Y.; Zana, R. *Langmuir* **1995**, *11*, 1448–1456.
(54) Weihs, D.; Danino, D.; Pinazo-Gassol, A.; Perez, L.; Franses, E. I.; Talmon, Y. *Colloids Surf., A* **2005**, *255*, 73–78.
(55) Ghafouri, R.; Bruinsma, R. *Phys. Rev. Lett.* **2005**, *94*, 138101.
(56) Oda, R.; Huc, I.; Schmutz, M.; Candau, S. J.; MacKintosh, F. C. *Nature* **1999**, *399*, 566–569.
(57) Brizard, A.; Aime, C.; Labrot, T.; Huc, I.; Berthier, D.; Artzner, F.; Desbat, B.; Oda, R. *J. Am. Chem. Soc.* **2007**, *129*, 3754–3762.
(58) Ziserman, L.; Harries, D.; Mor, A.; Danino, D., submitted.

**SUPPORTING INFORMATION**

## 1. Materials

### Peptide synthesis and purification

$C_{12}$-$\beta_{12}$ belongs to a new synthetic library of pseudo-peptides termed oligo-acyl-lysyl (OAK), designed to mimic the structure and function of host defense peptides (HDPs) [1-3]. Fmoc $C_{12}$-$\beta_{12}$ was synthesized by solid phase peptide synthesis using a fully automated, programmable peptide synthesizer (Applied Biosystems 433A) as described before. Products were purified to > 95% chromatographic homogeneity by reverse-phase high-pressure liquid chromatography (HPLC, Alliance Waters) on C18 columns (Vydac, 250mm x 4.6 or 10mm) using a linear gradient of acetonitrile in water (1% per min) containing 0.1% TFA. Composition was validated by mass spectrometry (ZQ Waters). Compounds were stored as lyophilized powders at -20 °C. $C_{12}$-$\beta_{12}$ molecule contains two primary amine groups of the two lysine side-chains. Their ionization pK is about 10.7, therefore, they are positively charged in neutral pH. The lysines' $C^{\alpha}$ are the two chiral centers of the molecule. The counterion is trifluoroacetate.

### Solution preparation

For time-resolution studies, $C_{12}$-$\beta_{12}$ solutions were prepared by dissolving the powder in Milli-Q purified water, vortexing, and brief sonication, followed by two hours at 90 ºC, then incubation at room 25 ºC. Most experiments were done 3 mM, ~ 10-fold the CAC. In this preparation route, assembly into closed nanotubes takes 4 months.

## 2. Methods

### Cryogenic-transmission electron microscopy (cryo-TEM)

To ensure microstructural preservation during specimen preparation, vitrified specimens were prepared in the semi-automated Vitrobot (FEI), or the controlled environment vitrification system (CEVS). Both are closed chambers enabling sample preparation at well-controlled temperatures and at 100% relative humidity. Specimens were prepared by placing a 5-8 µl sample drop onto a perforated carbon film supported on a TEM copper grid held by tweezers. The drop was thinned (blotted) to produce a thin

specimen film, plunged into liquid ethane at its freezing point (-183 °C) to create a vitrified specimen, and transferred to liquid nitrogen (-196 °C) for storage until examination. Vitrified specimens were examined at cryogenic temperatures in a Philips CM120 (Philips, The Netherlands) or Tecnai T12- G$^2$ (FEI, The Netherlands) TEMs, operated at 120 kV, using Oxford CT3500 or Gatan 626 cryo-specimen holders maintained below -175 °C. Images at magnifications up to 50K were recorded digitally as described before [4], on a Gatan MultiScan 791 CCD camera (CM120) or a Gatan 2kx2k UltraScan 1000 camera. Both cameras are equipped with phosphorous scintillators, to achieve the high sensitivity required for low-dose imaging and minimizing electron-beam radiation damage.

**Negative-staining TEM (NS-TEM)**

NS-TEM samples were prepared on copper 400 mesh grids coated with nitro-cellulose membrane, and a thin carbon layer, as described [5]. The grids were placed on ~20 µl sample drops for 2 min. Excess solution was removed by blotting with a filter paper. Then, each specimen was washed twice in filtered (0.22 µm Millipore filters) 2% uranyl acetate, fixed by placing the grid on a 20 µl drop of 2 % uranyl acetate for 2 min, blotted again, air dried, and kept dry until examination at room temperature.

**Surface-tension measurements**

The critical aggregation concentration (CAC) was calculated from surface tension measurements done by the *maximum bubble pressure method* (MBPM) [6-7] using a fine capillary (0.223 mm in diameter) minimally immersed (about 1 mm) in the examined solution. The pressure variation in the capillary during bubble formation was monitored by a sensitive pressure transducer (Baratron type 223BD, MKS Instruments Inc.) and the maximum bubble gauge pressure ($\Delta P_{max}$) was used to calculate the surface tension using the Young-Laplace equation:

$$\sigma = \frac{\left(\Delta P_{\max} - \rho \cdot g \cdot h\right) \cdot R}{2}$$

where $\sigma$ is the surface tension, $R$ the inside capillary radius, $\rho$ the liquid density, $g$ the acceleration of gravity, and $h$ the capillary depth of immersion. The CAC, calculated from the break in the surface tension vs. concentration plot, was found to be 0.35 mM.

**Differential scanning calorimetry (DSC)**

Solutions were scanned with the Microcal VP-DSC-ER calorimeter (Microcal Inc., Northampton, MA) at a scan rate of 0.5 ºC per minute. The reported results of heat capacity, *Cp*, versus temperature refer to heating scans. The data was analyzed using the Origin 5.0 software supplied by the DSC manufacturer (Microcal).

**Dynamic light scattering (DLS)**

DLS experiments were performed using a BI-200SM System (Brookhaven Instruments Corp., USA). A Compass 415 M solid-state laser (Coherent, USA), generating monochromatic green light of 532 nm wavelength passed through the samples, and the intensity of light scattered at 90° was measured by a photomultiplier tube. The average hydrodynamic radius $R_h$ of the assemblies was calculated using the Stokes-Einstein equation: $D = kT/6\pi\eta R_h = \lambda/q^2$ where $k$ is the Boltzmann constant, $\eta$ the solvent viscosity, and $T$ the absolute temperature [8-9]. The autocorrelation functions were analyzed using CONTIN [10]. Data acquisition was carried out for 5 min at predetermined controlled temperatures, keeping the number of photons per second within a range of 500-1000 kcps. Particle size distribution was displayed by number weighting. DLS measurements were consistent with the existence of only spherical micelles at 40 and 55 °C, with mean micellar diameter of 5.62 nm.

**Powder X-ray scattering (XRD)**

Powder X-ray diffraction measurements were carried out on a Philips PW 3020 powder diffractometer equipped with a graphite crystal monochromator (Philips, The Netherlands), at Cu K$\alpha$ radiation ($\lambda$=0.154 nm), 40 kV and 40 mA. Approximately 100 mg of sample powder was loaded onto an aluminum plate. A few drops of distilled water were added to form thin, homologues layers of material on the sampling plate. After drying, samples were scanned at Bragg angles of $2^o$ - $35^o$ in steps of $0.02^o$ per second.

**Small-angle neutron scattering (SANS)**

SANS measurements were made on the NG-3 (30 m) beamline at the National Institutes of Standards and Technology (NIST) in Gaithersburg, MD. Samples were prepared in $D_2O$ and studied at 25°C in 2 mm quartz cells. The scattering spectra were corrected and placed on an absolute scale using calibration standards provided by NIST. Data are shown for the absolute intensity $I$ versus the wave vector $q = (4\pi/\lambda)\sin(\theta/2)$, where $\lambda$ is the wavelength of incident neutrons and $\theta$ is the scattering angle.

**Fourier transform infrared spectroscopy (FTIR)**

FTIR measurements of dry powders and aqueous solutions were performed at 25ºC with Equinox 55 and Tensor 27 spectrometers (Bruker Optics, Billerica, MA, USA), respectively. IR absorption spectra within a range of 1000-4000 $cm^{-1}$ were measured at 1 $cm^{-1}$ resolution. Data analysis was performed with the OPUS$^{TM}$ software. For the dry powder experiments, KBr lenses were used. 2 mg of the lyophilized compound was stored with silica gel for at least 48 hrs before examination to remove traces of water. Subsequently, KBr pellet samples were prepared by mixing the material with *ca.* 100 mg KBr dry powder and manually pressing them together by a homemade vise to form thin "lenses", which then immediately were transferred into the instrument for examination. The comparable aqueous solutions were examined by an Attenuated Total Reflectance (ATR) cell with small sample capacity (about 30 µl). The ATR crystal used is zinc selenide (ZnSe) [11].

### 3. Supporting Data

A

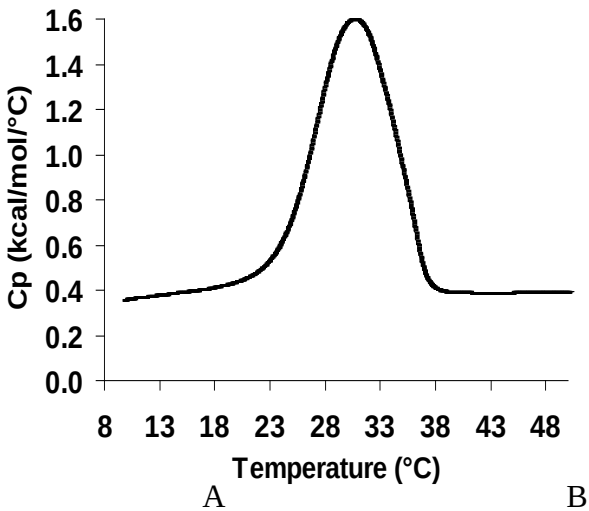


A B

B

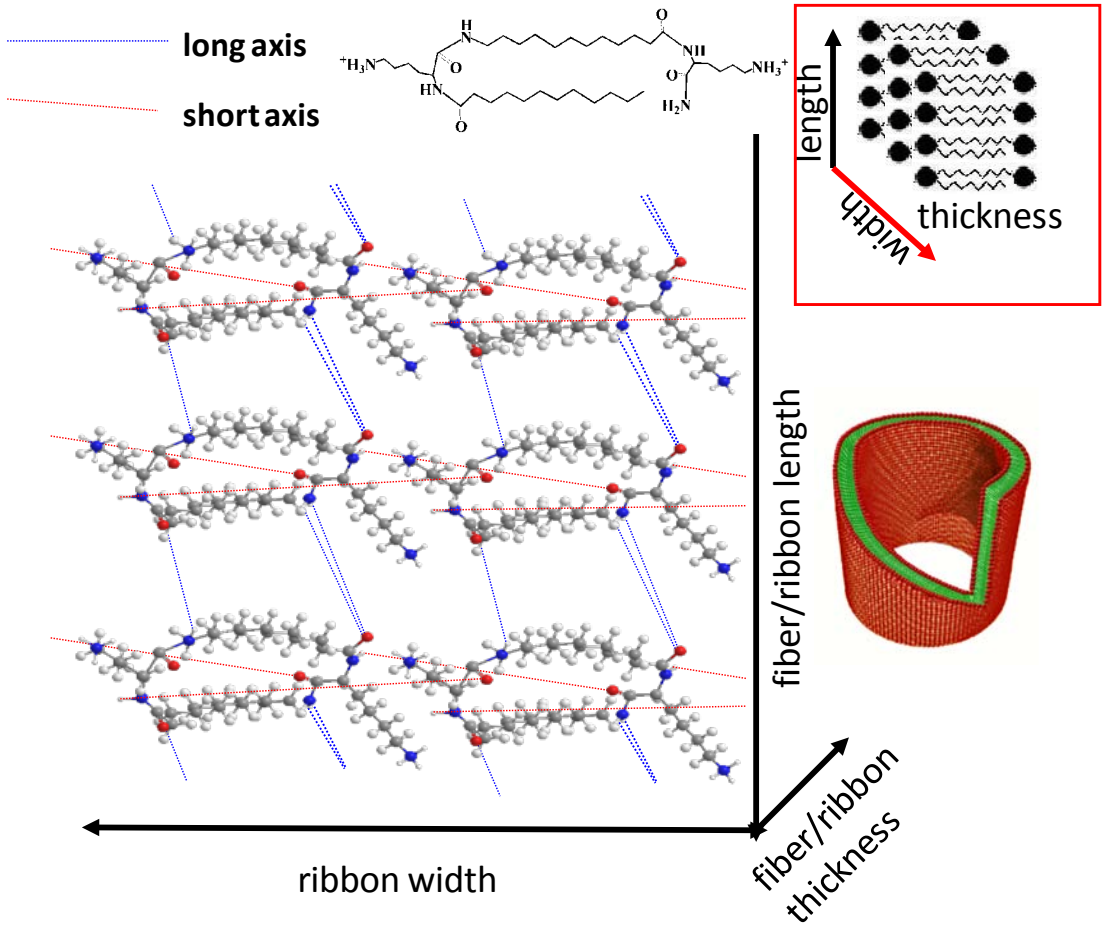

**Figure S1:** (A) The DSC plot of heat capacity (Cp) vs. temperature peaks at 30.6 °C. Integration of the endothermic peak yields $\Delta H$ = 10.3 kcal/mol (43 kJ/mol), which is comparable with values reported in the literature for lipid molecules. (B) The complete model for the organization of $C_{12}$-$\beta_{12}$ in the gel phase. The model assumes two sets of hydrogen bonds holding the molecules into fibers, and associating the fibers into ribbons.

References


(1) Radzishevsky, I. S.; Rotem, S.; Bourdetsky, D.; Navon-Venezia, S.; Carmeli, Y.; Mor, A. *Nature Biotechnology* **2007**, *25*, 657-659.
(2) Radzishevsky, I. S.; Kovachi, T.; Porat, Y.; Ziserman, L.; Zaknoon, F.; Danino, D.; Mor, A. *Chemistry & Biology* **2008**, *15*, 354-362.
(3) Rotem, S.; Mor, A. *BBA* **2009**, *1788*, 1582-1592.
(4) Danino, D.; Bernheim-Groswasser, A.; Talmon, Y. *Colloid Surface A* **2001**, *183*, 113-122.
(5) Hamley, I. W.; Castelletto, V.; Moulton, C.; Myatt, D.; Siligardi, G.; Oliveira, C. L. P.; Pedersen, J. S.; Abutbul, I.; Danino, D. *Macromol Biosci* **2010**, *10*, 40-48.
(6) Hallowell, C. P.; Hirt, D. E. *Journal of Colloid and Interface Science* **1994**, *168*, 281-288.
(7) Shalel, S.; Streichman, S.; Marmur, A. *Journal of Colloid and Interface Science* **2002**, *255*, 265-269.
(8) Lau, C.; Bitton, R.; Bianco-Peled, H.; Schultz, D. G.; Cookson, D. J.; Grosser, S. T.; Schneider, J. W. *Journal of Physical Chemistry B* **2006**, *110*, 9027-9033.
(9) Roy, S.; Dey, J. *Bulletin of the Chemical Society of Japan* **2006**, *79*, 59-66.
(10) Provencher, S. W. *Biophys J* **1976**, *16*, 27-41.
(11) Stuart, B. *Biological applications of infrared spectroscopy*; John Wiley & sons: Chichester, 1997.